1   # A Lagrangian analysis of cold cloud clusters and their life cycles with

2   # satellite observations

3

4   Rebekah Bradley Esmaili

5   *Dept. of Atmospheric and Oceanic Science, University of Maryland, College Park, Maryland*

6   Yudong Tian

7   *Earth System Science Interdisciplinary Center, University of Maryland, College Park, Maryland*

8   Daniel Alejandro Vila

9   *National Institute for Space Research (INPE), São José dos Campos, Brazil*

10   Kyu-Myong Kim

11   *NASA Goddard Space Flight Center, Greenbelt, Maryland*

12

13

16

17

18   Corresponding author address:

19   Rebekah B. Esmaili

20   3417 Computer & Space Sciences Blg.

21   College Park, Maryland 20742-2425

22   Tel: (301) 614-6537

23   Email: bekah@umd.edu

24 ABSTRACT

25 Cloud movement and evolution signify the complex water and energy transport in the

26 atmosphere-ocean-land system. Detecting, clustering, and tracking clouds as semi-

27 coherent cluster objects enables study of their evolution which can complement climate

28 model simulations and enhance satellite retrieval algorithms, where there are large gaps

29 between overpasses. Using an area-overlap cluster tracking algorithm, in this study we

30 examine the trajectories, horizontal extent, and brightness temperature variations of

31 millions of individual cloud clusters over their lifespan, from infrared satellite

32 observations at 30-minute, 4-km resolution, for a period of 11 years. We found that the

33 majority of cold clouds were both small and short-lived and that their frequency and

34 location are influenced by El Niño. More importantly, this large sample of individually

35 tracked clouds shows their horizontal size and temperature evolution. Longer lived

36 clusters tended to achieve their temperature and size maturity milestones at different

37 times, while these stages often occurred simultaneously in shorter lived clusters. On

38 average, clusters with this lag also exhibited a greater rainfall contribution than those

39 where minimum temperature and maximum size stages occurred simultaneously.

40 Furthermore, by examining the diurnal cycle of cluster development over Africa and the

41 Indian subcontinent, we observed differences in the local timing of the maximum

42 occurrence at different life cycle stages. Over land there was a strong diurnal peak in the

43 afternoon while over the ocean there was a semi-diurnal peak composed of longer-lived

44 clusters in the early morning hours and shorter-lived clusters in the afternoon. Building

45 on regional specific work, this study provides a long-term, high-resolution, and global

46 survey of object-based cloud characteristics.

47

Esmaili et al., 2016   2

48   1. Introduction

49   Clouds are the most visible vital sign of the atmosphere's dynamic water and energy

50   transfer. They are responsible for the latent heat release that drives the atmospheric

51   circulation. Their transport of water in the form of moisture and precipitation is critical

52   for the Earth's hydrological cycle. On sub-synoptic scales, the cloud systems' movement,

53   evolution, and spatial and temporal characteristics are remarkably turbulent and complex.

54   The Lagrangian framework is an effective approach to study cloud clusters. Treating each

55   cloud as an object across it's lifespan produces useful information on the evolution of

56   cloud systems' properties, which is not available from the Eulerian view [Machado et al.,

57   1998]. Renewed interest in cloud object-based evolution is partly due to the advancement

58   of satellite-based multi-sensor high-resolution precipitation estimates [Li et al., 2015].

59   Currently, these estimates rely heavily on observations from passive microwave (PMW)

60   sensors aboard polar-orbiting satellites [Kummerow et al., 2000; Joyce et al., 2004;

61   Huffman et al. 2007; Huffman et al. 2013]. These PMW-based estimates are relatively

62   accurate, but they do not correlate well with surface observations when precipitation is

63   very light, very heavy, or over saturated land surfaces, particularly during winter months

64   [Ebert et al., 2007]. Additionally, these data have large spatial and temporal gaps.

65   One way to bridge these coverage gaps is to use cloud system advection information

66   derived from high-resolution infrared observations to continuously "morph" the PMW-

67   based rainfall [Joyce et al., 2004; Kubota et al., 2007; Xie and Xiong, 2011]. These

68   approaches have been proven effective and are being incorporated into Integrated Multi-

69   satellitE Retrievals for GPM [IMERG; Huffman et al., 2013], the next-generation, Global

70 Precipitation Measurement (GPM; Hou et al., 2014) era product suite. However, the

71 accuracy of the PMW-based estimates is also influenced by the life cycle stage [Tadesse

72 and Agnastou, 2011]. Developing a more detailed understanding of evolution can provide

73 additional context.

74 Another critical application is the evaluation and diagnosis of global models. Currently

75 atmospheric models still unrealistically reproduce observed precipitation [Ebert et al.,

76 2007; Stephens et al. 2010]. The conventional Eulerian validation gives the spatial and

77 temporal statistics on each individual grid box, which is the accumulation of many

78 different cloud systems at various life stages. A Lagrangian comparison of modeled and

79 observed cloud evolution statistics could produce additional insight on the modeling of

80 individual cloud-precipitation processes [Boer and Ramanathan, 1997].

81 In the past, studies that combined infrared satellite-based cloud cluster tracking with

82 Tropical Ocean Global Atmosphere (TOGA) field campaigns to examine cloud evolution,

83 anatomy, and development conditions [Williams and Houze, 1987; Chen and Houze,

84 1997]. On larger scales, Mesoscale Convective Systems (MCS) have in particular been

85 studied due to their ease of detection in radar and satellite images and destructiveness

86 [Maddox, 1980; Laing and Fritsch, 1997; Blamey and Reason, 2011]. MCS display

87 regularity in their life cycles, enabling Machado et al. [2004] to develop a statistical life

88 cycle model to predict MCS propagation with good forecasting skill.

89 As global, long-term, quality controlled IR data and precipitation data become available

90 [e.g., Janowiak et al., 2001; Joyce et al., 2004], it becomes feasible to extend IR-based

91 cloud tracking beyond regional scales and expand the scales of observed phenomena. By

92   following a large number of cloud clusters on the global scale for over 11 years, we will

93   be able to understand more systematically their large-scale dynamical and statistic

94   characteristics.

95   In this paper, we present a near-global (60°S-60°N), high-resolution (30-minute, 4-km),

96   long-term (11-year) study of cloud cluster tracks, life cycle evolution, and diurnal cycle.

97   The high-resolution data used for the study and the methodology for storm tracking are

98   described in Section 2 and 3, respectively. Section 4 presents the results, followed by

99   summary and discussions in Section 5.

100   2. Data

101   For our study, we use the NCEP/CPC a 4-km, half hourly infrared (IR) brightness

102   temperature dataset [Janowiak et al., 2001]. The dataset is merged from all available

103   geostationary satellites (GMS, Meteosat-5, Meteosat-7, GOES-8 and GOES-10) to form

104   near-global (60°N-60°S) coverage on a uniform latitude-longitude grid. We used 11 years

105   of data from 2002 to 2012 for our study.

106   We have performed additional quality control of the IR data. There are gaps in the IR

107   data in regions covered by the GMS satellite in the Western Pacific (120°-170°E), so we

108   filled the missing data by interpolating the preceding and following 30-minute snapshots,

109   to produce more seamless coverage. Our tests show that this interpolation helps to

110   prevent early termination of the cloud lifespan due to missing data.

111   3. Methodology

112   The techniques for tracking clouds are mature and largely similar, albeit there are many

113   implementations. Most of those techniques involve IR geostationary satellite imagery to

114   follow classes of convective events. The primary dissimilarities in algorithms involve the

115   detection criteria, such as through the selection of brightness temperature or size

116   parameter thresholds [Carvalho and Jones, 2001; Morel and Senesi, 2002], usage of more

117   nuanced detection schemes [Lakshmanan, 2009], or the treatment of splits and merges

118   [Fiolleau and Roca, 2013].

119   In spite of a variety of implementations, Machado et al. [1998] found most of the life

120   cycle statistics are not overly sensitive to the tracking method used. For this paper, we

121   selected Forecast and Tracking the Evolution of Cloud Clusters [ForTrACC; Vila et al.,

122   2001] which has a single temperature and system size threshold and merges and splits are

123   treated as special cases for tracking systems (this will be explained in the Section 3.2).

124   ForTrACC's simplicity enabled us to capture a broader range of cloud species.

125   Tracking clouds involves the following two major steps:

126   *3.1. Identification using temperature and morphology*

127   Using brightness temperature thresholds to capture clouds has been used in past studies

128   and typically empirically derived to satisfy the research goals [e.g. Blamey and Reason,

129   2001; Velasco and Fritch, 1987; Williams and Houze, 1987]. In general, brightness

130   temperature detection thresholds vary between 235-255 K and tended to be subjectively

131   chosen. However, the cluster areal extent was found to the linearly dependent on cluster

132   threshold and thus not overly sensitive to the exact threshold chosen [Machado et al.

133   1992; Mapes and Houze, 1993].

134   To capture a variety of cloud clusters, we used a single 235 K brightness temperature

135   threshold, which in the upper atmosphere corresponds to a height of roughly 10 km (9

136   km) in the tropics (midlatitudes), which is well into the free atmosphere. Additionally, we

137   applied a minimum size threshold of 100 contiguous pixels (1,600 km^2 at the equator) at

138   all time steps, thus limiting the study to events at the upper bounds of mesoscale or larger.

139   We excluded smaller scale events because they would be more suitable for regional

140   studies. Figure 1 shows this selection criteria being applied to a typical IR snapshot. A

141   temperature range of 235-245 K have been used in the past to detect cloud clusters (e.g.

142   Williams and Houze, 1987; Mapes and Houze, 1993; Carvalho and Jones, 2001;

143   Machado et al., 2004); the colder threshold is utilized to avoid capturing frozen, high

144   altitude surfaces. The size threshold reduces the number of tracked clouds by filtering out

145   small-scale events and reducing the number of splits and merges. With only a

146   temperature threshold, a single time step can yield over 17,000 cloud clusters. Applying

147   the size threshold decreased to the number to 800-1000 events.

148   *3.2. Tracking using area overlap*

149   ForTrACC uses an area overlap technique to track the cloud clusters, both forward and

150   backward in time. If two cloud clusters identified in different time steps have any shared

151   pixels, they were considered the same system and assigned a family number. If more than

152   one match was found, the largest overlaping system was tracked.

153   Using infrared data, we show in Figure 2 a schematic of the area-overlap handling in

154   ForTrACC. The area overlap technique produces several cloud cluster merge scenarios:

155   one-to-one (continuous), one-to-many (split), many-to-one (merge), or no match

156 (initialization or dissipation). Most systems undergo merging or splitting in their life

157 cycle, the prior occurs before maturation, the latter more frequently towards the end of

158 the life cycle. Only one cluster is followed at each time step to keep features well defined.

159 When clusters split, the largest cloud continues to be tracked while the smaller split

160 clusters are treated as a new family and the lifetime clock is reset. All merging clusters

161 are considered a dissipation and their life cycle ends. ForTrACC's handling of split and

162 merge segments is different from earlier work; in other schemes, the segments remain

163 part of the cloud cluster system rather than considered a new systems [Mapes and Houze,

164 1993; Chen and Houze, 1996; 1997)].

165 A sample output of the resulting cloud cluster tracks are shown in Figure 3. In addition to

166 showing centroid location, statistics related to the size or areal extent, the mean

167 brightness temperature, and travel distance of the cluster are also calculated. Colder

168 temperatures indicate higher cloud tops while areal extent shows the relative scale of the

169 observed system. All clusters achieve a minimum temperature and maximum size, which

170 we use as criteria for developmental maturity in Section 4.5. We use this information to

171 study the ForTrACC-based cloud clusters' statistical properties, climatology, life cycle,

172 rainfall contribution, and diurnal cycle.

173   *3.3. Collocation of clusters with passive microwave rainfall estimations*

174 To examine the rainfall contribution of cloud clusters, we matched PMW precipitation

175 estimates from IMERG [Huffman et al., 2013] with spatially and temporally collocated

176 cloud clusters.

177   While TRMM-based products have a longer data record, GPM has global coverage so we

178   selected two months of data to examine (June and December 2014). Both datasets were

179   scaled to a common grid (0.1° x 0.1°) and the available rainfall totals were summed for

180   clusters at various life cycle stages.

181   4. Results

182   *4.1. Mean trajectories and statistical properties of cloud clusters*

183   Tracking on the global scale builds on regional studies and enables us to document many

184   fundamental statistical characteristics of cloud clusters. At any instant, there are on

185   average 800 clusters larger than 1,600 km^2 in the Earth's atmosphere between 60°S and

186   60°N. Figure 4 shows the global distribution of clusters with lifetimes between 6 and 9

187   hours, for both December through February (DJF) and June through August (JJA). The

188   mean trajectories are calculated by averaging the endpoints of all cluster centroids that

189   initiate at the same 2° x 2° binned latitude and longitude coordinates. The colors

190   represent the net zonal direction of the flow.

191   Regarding the zonal average distance travelled by 6-9 hour lifetime clusters in Figure 4,

192   we found that cloud clusters travel further in the Northern Hemisphere during DJF; the

193   average distance traveled peaks at 644.8 km at 36°N, which is likely due to influence of

194   the climatological jet stream on development and propagation. In the Southern

195   Hemisphere the maximum occurs near 52°S at a lower 419.8 km. Movement in the

196   tropics doesn't vary drastically from each season, but the peak (189.1 km) occurs in JJA

197   at 12°N. This is in part due to the persistence of the ITCZ and African Easterly Wave

198   activity.

199   Cloud clusters can last from a few hours up to two days, and their sizes range from our

200   minimal threshold to more than 10^6 km^2 (Figure 5). Most of the clusters are short-lived

201   and small (Figure 5a), with 90% of the clusters detected having a size less than 49,275

202   km^2 and a lifetime less than 5 hours. The cluster lifetime distribution follows roughly a

203   log-linear distribution while the cluster size distribution appears to be lognormal at

204   certain scales, the latter being consistent with some past findings [Machado et al. 1992;

205   Mapes and Houze, 1993] but different from others [Lovejoy and Schertzer, 2006]. Figure

206   5b shows the kernel density estimate [Rosenblatt, 1956; Parzen, 1962], a non-parametric

207   estimate of the probability density of maximum areal extent of each cluster across several

208   lifetime bins.

209   Overall, Figure 5 shows that the frequency of cluster lifetime and size are proportional.

210   This is similar to the results from Chen et al. [1997], who show a linear correlation

211   between the count of tropical cloud clusters with respect to maximum size and lifetime in

212   the western Pacific. This reinforces that shorter lived events tend to remain small in scale

213   while longer-lived ones achieve greater horizontal scales.

214   These results can be compared with event tracking based on model data [e.g. Bengtsson

215   et al., 2006; Bengtsson et al., 2009; Hoskins and Hodges, 2001; Neu et al., 2013; Sinclair,

216   1994]. Modelling studies typically use vorticity or sea level pressure as the defining

217   feature of midlatitude cyclone storm tracks. Coupled with lower temporal resolution data,

218   this can result in smoother tracks and are larger and longer-lived than the ones shown in

219   Figure 4. The differences are due to tracking definitions but may also be due to the

220   prevalence of lighter rainfall typical in models as compared with observations [Stephens

221   et al., 2010].

222   *4.2. Cloud cluster climatology*

223   On the global scale, the clusters exhibit many systematic spatial and temporal

224   characteristics, as seen in the seasonal climatology map of clusters (Figure 6). The map

225   produced is the frequency of clusters at their maximum areal extent for each 2° x 2°

226   latitude-longitude bin. During DJF, the intertropical convergence zone (ITCZ) is closer to

227   the equator and South Pacific convergence zone is intensified. There is increased activity

228   from the midlatitude storm tracks across the North American west coast and Europe. In

229   JJA, tracks capture the northward placement of the ITCZ, Atlantic coastal storms, and the

230   East Asian monsoon. Less activity is found in proximity of the semi-permanent high

231   pressure systems (e.g. Pacific and Bermuda highs in JJA). Artifacts in south Pacific (40°-

232   60°S, 120°-160°W) are due to calibration differences between geostationary platforms

233   and the interface of the half-hourly and hourly sampling regions of the Geostationary

234   Meteorological Satellite between 120°-170°E. Note that in Figure 6a, we excluded data

235   from DJF 2006 from 120°-170°E due to intermittent noisy brightness temperature data in

236   this region.

237   The frequency also reveals some regional subtleties in Figure 6b. Over the Southeast-

238   Asia islands in the western Pacific Ocean, there are roughly twice as many clusters along

239   coastlines than the surrounding oceanic areas. This region's combination of topography,

240   land-sea thermal contrast, and available moisture generates storms that are both large in

241   scale and deep, making it it is one of the rainiest places on earth in TRMM-based object

242   studies [Houze et al., 2015].

243 Interestingly, a high count of clusters does not necessarily correlate with intense rainfall.

244 Outside the ITCZ, the Amazon, the Asian monsoon, and West African monsoon are

245 among the most active continental regions in terms of cluster frequency. However,

246 TRMM-based studies have shown objects tend to be moderate strength and larger scale in

247 the Amazon while the latter two regions are composed of deep convection [Zipser et al.

248 2006; Houze et al., 2015]. In the Amazon, rainfall features have a lower mean height than

249 those over the Asian and African monsoon regions and warm rain tends to be the greatest

250 contributor of rainfall [Liu and Zipser, 2008]. While not shown, statistically we found

251 that clusters in our study were typically larger, colder, and longer-lived over Western

252 Africa and the Indian Subcontinent (JJA), whereas shorter-lived, moderate sized clusters

253 tended to occur over the Amazon (DJF).

254 Compared to results based on reanalysis-based tracking results, the JJA cluster counts

255 shown in Figure 6b resemble vorticity-based African Easterly [Thorncroft and Hodges,

256 2001]. In both studies, intiation maxima occur along the West Africa coast and Ethiopian

257 highlands as well as over the Pacific, downstream of Central America. We visually

258 observed that our IR-based tracks are noisier than reanalysis derived ones and are less

259 exclusive. Tracking with six-hourly data can skew results towards stronger, longer-lived

260 events, and can miss younger events.

261   *4.3. Inter-annual variability*

262 There is significant inter-annual variability in cluster occurrence, particularly between El

263 Niño and La Niña years. Figure 7 shows the composite of frequency difference of cluster

264 overpasses at their maximum size during the El Niño phases for 11-years of DJF, binned

265   by 2° x 2° latitude-longitude boxes. This was produced by subtracting the annual average

266   frequency of cluster occurrence during warm phases from the annual average of cool

267   phases. Only seasons with weak, moderate, or strong phases based on the NINO3.4 sea

268   surface temperature anomaly index are included.

269   El Niño has an expected effect on the frequency of cloud clusters in the tropics: more

270   clusters are observed near the equator during the warm phase in the central pacific

271   (160°E-160°W) and in the western pacific (110°-160°E) during the cool phase. However,

272   teleconnections can also be observed; there is an increase in occurrence over the

273   Northwest United States (25-55°N, 100-120°W) and Indian Ocean (10°S-10°N, 40°-

274   80°E) and a decrease in the Atlantic basin (10°S-10°N, 60°-10°W) during El Niño. Teng

275   et al. [2014] have shown that there are both increases in cloud cluster occurrence as well

276   as their likelihood of forming tropical cyclones in the western North Pacific during El

277   Niño.

278   *4.4. Life cycle of cloud clusters*

279   The advantage of continuous Lagrangian tracking is that it allows us to examine

280   systematically the clusters' full life cycle and the associated evolution of their

281   characteristics. Figures 8 and 9 show how the size and brightness temperature of clusters

282   evolve throughout their lifespan. Each curve represents the average of the aggregated

283   clusters that lived to the same age. For clarity, clusters that merged into or split off from

284   existing clusters were not included in Figures 8 and 9. Shorter curves represent brief

285   events while longer lines represent clusters with longer lifespans. The observed mean life

286   cycles have a well-defined stages of development – initial detection, intensification,

287 maturity, and decay. This can be seen in both their size evolution (Figure 8) and

288 brightness temperature evolution (Figure 9). With respect to size, clusters initiate, grow,

289 and achieve their areal maximum closer to the end of their life cycle (Figure 8). At their

290 size maximum, longer-lived clusters can double or triple their initial areal extent. Shorter-

291 lived ones undergo rapid decay early in their cycle. In contrast, during their brightness

292 temperature life cycle, clusters cool to a minimum and then begin to warm for the rest of

293 the life cycle (Figure 9). While an individual clusters' evolution usually appears erratic

294 and unpredictable, collectively their mean behavior computed from the ensemble of 10

295 million clusters shows regularity.

296 The minimum brightness temperature is reached at an earlier point in the clusters life

297 cycle than the size maximum. This could be due to overshooting tops, which reach deep

298 into the troposphere or lower stratosphere first, and then expand to form anvils as they

299 cool, and thus attaining their minimum brightness temperature before their maximum

300 areal extent. Additionally, clusters at their maximum areal extent produce cirrus shields

301 can also conceal the true extent of the clusters underneath.

302 On the global scale, the life cycle evolution shows substantial differences over

303 contrasting seasons and land surfaces. Due to their similarity, in Figures 8 and 9 regions

304 are divided into seasons along the ±25° latitude line, where Northern and Southern

305 winters (summers) are during DJF and JJA (JJA and DJF), respectively. The tropics use

306 data from both seasons. Generally, growth is more vigorous in summer than in winter

307 (e.g., compare Figures 8b and 8f, Figures 9b and 9f), over land than over ocean (e.g.,

308 compare Figures 8a and 8b to Figures 9a and 9b). In addition, the wintertime clusters are

309 much larger than summertime (e.g., Figures 8a and 8e). In the summer, the midlatitude

310   size curves (Figures 8a and 8b) are more similar to the tropics (Figures 8c and 8d).

311   Regarding brightness temperature, there is a larger spread during the summer (Figures 9a

312   and 9b) and in tropics (Figures 9c and 9d) than during the winter for both land and ocean

313   (Figures 9e and 9f). Clusters in the tropics (Figures 9c and 9d) are significantly cooler

314   than higher latitudes due to deep convection (Figures 9a and 9b).

315   The peaks in Figures 8 and 9 were fitted to a quadratic linear regression model to show

316   the general trend of size and temperature maturity across different lifetimes. Shorter-lived

317   clusters tended to be already at maturity at the time of detection – that is, the shortest

318   lines in Figures 8 and 9 show that these clusters total area decreased and temperatures

319   rapidly increased. For longer-lived clusters, the timing of the maximum areal extent and

320   minimum temperature was asynchronous and larger than that for shorter-lived events. We

321   will examine some of the implications of this in the following sections.

322   *4.5 Cloud Clusters and Rainfall*

323   In raining cloud clusters, the differences in the timing of the minimum brightness

324   temperature and maximum size contribute varying amounts to total precipitation. In

325   Figure 10, we identified several distinct life cycle stages (initiation, mixed maturity,

326   minimum brightness temperature, maximum size, and dissipation) and the instantaneous

327   total volumetric rainfall that is attributed to each rain rate bin. Using the procedure

328   detailed in Section 3.3, this was determined by collocating the cloud clusters with

329   available microwave-only rainfall estimations from IMERG [Huffman et al., 2013], for

330   June and December 2014.

331   Due to the lower temporal resolution of polar orbiting satellites, most clouds could only

332   be sampled once, so results are examined in a statistical sense rather than as totals by

333   individual objects. Here we define the minimum temperature (maximum size) as the

334   lowest average temperature (largest areal extent) achieved by a clusters. We also divide

335   contribution into two mutually exclusive maturity states, synchronous and asynchronous

336   occurrence of minimum temperature and maximum areal extent. The prior is denoted as

337   mixed maturity, while the latter is broken down into the two stages of its variables.

338   Collectively, the figure shows the rainfall contribution of the beginning, mature, and final

339   life cycle stage.

340   Initially, raining clusters are composed of lighter rain and produce less of it. As

341   development continues, they produce larger volumes of rain as the areal extent of the

342   cloud increases. It is interesting that in all cases, mixed maturity clusters contribute less

343   rainfall than those with asynchronous stages. These cases tended to be shorter lived on

344   average (1.9 hours) than those with larger differences in timing (2.9 hours).

345   There are seasonal differences in these values. The winter midlatitudes (Figurs 10b and

346   10e) produced more overall rain than their corresponding summer hemisphere (Figures

347   10a and 10f) and were more heavily skewed towards lighter rainfall. The tropics had less

348   seasonal variation in rainfall contribution (Figures 10c and 10d).

349   Precipitation retrieval algorithms may benefit from incorporating information on the life

350   cycle stage, season, and hemisphere of the IR cloud cluster. In morphing techniques, the

351   shape and intensity of rain clusters is held constant between overpasses [Joyce et al.,

352   2004], while in figures 8 and 9 we show that both horizontal size and temperature growth

353   rates are not constant during cloud cluster evolution. Biases in hourly rain volume

354   estimates vary across life cycle stages, lifetimes, and precipitation algorithm [Tadesse

355   and Anagnostou, 2009]. Knowing the age of the cloud could be useful in devising the

356   next-generation multi-sensor algorithms.

357   *4.6 Diurnal cycle of cluster evolution*

358   By continuously tracking cloud clusters, we can study when and where they reach their

359   life cycle milestones. Figure 11 shows the local solar time (LST) of the maximum in the

360   frequency of cluster initiation. This was calculated from frequency maximum at each

361   hourly, 2° x 2° bin for clusters with a lifetime greater than two hours. Over land, peak

362   cloud initiation occurs in the afternoon, especially in the summer hemisphere. Over the

363   ocean, there is greater prevalence of early morning and afternoon clouds, but the timing

364   of peak activity depends on region. This double peak was also previously found in the

365   West Pacific warm pool by Chen and Houze (1997). To examine these differences in

366   context of development stage, we examine two regions centered over West Africa (0-

367   40°N, 50°W-20°E) and the South Asian peninsula (0°-30°N and 60°-90°E).

368   In Figure 12, we examine the kernel density of the LST by cluster life cycle stage in these

369   two regions for both seasons. Over land, there is a strong diurnal cycle and a lag in the

370   local timing of initiation, minimum temperature, and maximum size. The timing

371   differences are much smaller over the ocean in both regions and there is a semi-diurnal

372   cycle over the ocean. The timing of peak initiation over land is earlier in the South Asian

373   region (1300 LST) than in the Western Africa region (1500 LST). This is possibly due to

374   the windward side of the Indian subcontinent skewing the the population to lower

375   initiation times. Over the ocean, the early morning peaks have similar timing (0200 LST),

376   but the afternoon peak in Western Africa is earlier (1100 versus 1300 LST). Kikuchi and

377   Wang [2008] observed this semi-diurnal cycle over the Pacific, Indian, and Atlantic

378   Oceans in empirical orthogonal modes of TRMM datasets. We can take advantage of the

379   known lifetime and further inspect the duration of these cloud clusters at different times

380   of the day.

381   In Figure 13, we show the kernel density for the LST grouped by the three-hourly binned

382   lifetime. Over land, the timing differences were delayed by not more than an hour for all

383   lifetime groups. Shorter-lived clusters (those with lifetimes 6 hours or less) had a sharper

384   peak than longer-lived events (those with lifetimes greater than 6 hours). There are trivial

385   differences in the onset of short versus long-lived events in the South Asia region than

386   over West Africa.

387   However, over the ocean, longer-lived clusters had a greater tendency to occur in the

388   early morning hours, peaking between 0300-0400 and 0400-0500 LST in South Asia and

389   West Africa, respectively. Shorter-lived events peaked both in the early morning and

390   afternoon, but were the primary type in the afternoon afternoon between 1200-1300 LST

391   for both regions. In South Asia, the maxima of short-lived clusters precede that of long-

392   lived ones by an hour, partly due to rapid growth and decay of isolated convective cells

393   which upon visual inspection are more numerous in this region than in West Africa.

394   These results are interesting in light of previous examination of TRMM precipitation

395   features, which show that nocturnal storms are more intense over the ocean while over

396   land the strongest storms are observed during the day [Zipser, 2006]. In summary, the

397 oceanic semi-diurnal cycle can be understood to be composed of not just two different

398 size classes, but as cloud clusters with differing lifetimes as well.

399 Expanding on the study by Chen and Houze (1997), our results show that their results

400 extend beyond the West Pacific to other regions and over longer time periods. Chen and

401 Houze found that large scale, long lived clusters follow a two-day cycle. The formation

402 of long-lived clusters suppresses subsequent development in that area due to dry

403 downdrafts from strong storms and the reduction in sea surface temperatures due to cloud

404 canopy shading. Examining the development-suppression cycle of cloud clusters in other

405 oceanic regions could be an interesting future direction for this work.

406   *5. Summary and Discussion*

407 In this study, we tracked cloud clusters on the global scale to study the climatology and

408 life cycles across a broad class of clusters using 11 years of the high-resolution, satellite-

409 based globally merged cloud brightness temperature data. We examined the trajectories,

410 climatology, life cycles, and diurnal cycle of clusters in context of their life cycle stage

411 and lifetime.

412 We found that the vast majority of clusters are short lived and small, demonstrating the

413 need to work with high-resolution data to fill in coverage gaps. Differences in the shapes

414 and scales of life cycle curves reflect the variety of clouds captured and show that

415 evolution is a complex process. Development over the oceans is less intense compared to

416 land, where strong thermal contrast, orography, and aerosols can influence evolution. We

417 observe a larger lag in the occurrence of minimum temperature and maximum size for

418 longer-lived cloud clusters, particularly over land. The diurnal cycle of cloud clusters

419   over the South Asia and West Africa revealed a strong diurnal peak over land and a semi-

420   diurnal cycle over the ocean, the latter of which showed greater prevalence of shorter

421   lived cloud clusters in the afternoon and dominance of longer lived events in the early

422   morning.

423   The capability for infrared data to reliably identify and track smaller scale convective

424   systems is an aspect in which global climate models still have difficulties [Stephens et al.

425   2010; Westra et al., 2014]. Thus, IR-based cloud tracking can be used to evaluate the

426   effectiveness of the downscaling abilities of models [Boer and Ramanathan, 1997]. On

427   the other hand, the infrared data can only depict the two-dimensional, cloud-top

428   characteristics of the clusters. To address the complex three-dimensional hydro-thermo-

429   dynamics of cloud systems, one has to combine observations from other satellites, such

430   as CloudSat and CALIPSO, with reanalysis data.

431   There are several limitations to this study that represent an area of ongoing work,

432   particularly regarding thresholds. Being too selective on size scales can exclude these

433   events; being too relaxed produces too many splits, which prematurely terminates the

434   cluster. Cold surfaces are a particular challenge, such as the Tibetan Plateau which is dry

435   in the northern winter. However, the relatively high frequency over this region in Figure

436   6a indicates mountain glacier surfaces are incorrectly being captured in this region. This

437   poses a challenge to other tracking studies, and mountainous areas are sometimes

438   removed from analysis [Neu et al., 2013]. As a future improvement, we could develop a

439   dynamic threshold criteria rather than a fixed brightness temperature value. [Hennon et

440   al., 2011].

441   Another challenge lies in the early termination of cloud clusters due to splits and mergers.

442   As clouds evolve, they continuously split and merge, each of which resets the lifetime

443   clock to zero. Only the largest, most well defined clusters avoid this in their lifetimes.

444   This is a limitation of this specific technique but the tracking algorithm could be refined

445   in the future to track features that do not have an easily defined shape, such as wintertime

446   midlatitudes storms or the movement of clouds that are part of atmospheric rivers.

447   In spite of such limitations, there are many promising areas of future work. The cluster

448   tracking provided in this study can be combined with other event based datasets, such as

449   the TRMM precipitation feature (TRMM-PF) dataset developed by Liu et al. [2008].

450   TRMM-PF has been extensively used to study the scale and intensity of rainfall events

451   and can infer life cycle stage from the vertical profiles obtained from the precipitation

452   radar. By combing TRMM-PF with our IR-based cloud tracks, rain features can be

453   studied in context of their entire life cycle and trajectory, overcoming the sampling limits

454   of polar orbiting satellites, to further our understanding of precipitating cloud systems.

455   ACKNOWLEDGEMENTS

463   REFERENCES

464   Adler, R. F. et al. (2003), The Version-2 Global Precipitation Climatology Project

465   (GPCP) Monthly Precipitation Analysis (1979–Present), *J. Hydrometeor.*, *4*(6),

466   1147–1167, doi:10.1175/1525-7541.

467   Boer, E. R., and V. Ramanathan (1997), Lagrangian approach for deriving cloud

468   characteristics from satellite observations and its implications to cloud

469   parameterization, *J. Geophys. Res.*, *102*(D17), 21383–21399, doi:10.1029/97JD00930.

470   Bengtsson, L., K. I. Hodges, and E. Roeckner (2006), Storm tracks and climate change, *J.*

471   *Climate*, *19*(15), 3518–3543.

472   Bengtsson, L., K. I. Hodges, and N. Keenlyside (2009), Will Extratropical Storms

473   Intensify in a Warmer Climate?, *J. Climate*, *22*(9), 2276–2301,

474   doi:10.1175/2008JCLI2678.1.

475   Blamey, R. C., and C. J. C. Reason (2012), Mesoscale Convective Complexes over

476   Southern Africa, *J. Climate*, *25*(2), 753–766, doi:10.1175/JCLI-D-10-05013.1.

477   Carvalho, L. M. V., and C. Jones (2001), A Satellite Method to Identify Structural

478   Properties of Mesoscale Convective Systems Based on the Maximum Spatial

479   Correlation Tracking Technique (MASCOTTE), *Journal of Appl. Meteorol*, *40*(10),

480   1683–1701, doi:10.1175/1520-0450.

481   Chen, S. S., R. A. Houze Jr., and B.E. Mapes (1996), Multiscale variability of deep

482   convection in relation to large-scale circulation in TOGA COARE, *Journal of the*

483   *Atmospheric Sciences*, *53*(10), 1380.

484   Chen, S. S., and R. A. Houze (1997), Diurnal variation and life-cycle of deep convective

485   systems over the tropical pacific warm pool, *Q.J.R. Meteorol. Soc.*, *123*(538), 357–

486   388, doi:10.1002/qj.49712353806.

487   Ebert, E. E., J. E. Janowiak, and C. Kidd (2007), Comparison of Near-Real-Time

488   Precipitation Estimates from Satellite Observations and Numerical Models, *Bull.*

489   *Amer. Meteor. Soc.*, *88*(1), 47–64, doi:10.1175/BAMS-88-1-47.

490   Fiolleau, T., and R. Roca (2013), An Algorithm for the Detection and Tracking of

491   Tropical Mesoscale Convective Systems Using Infrared Images From Geostationary

492   Satellite, *IEEE T. Geosci. Remot*, *51*(7), 4302–4315,

493   doi:10.1109/TGRS.2012.2227762.

494   Futyan, J. M., and A. D. Del Genio (2007), Deep Convective System Evolution over

495   Africa and the Tropical Atlantic, *J. Climate*, *20*(20), 5041–5060,

496   doi:10.1175/JCLI4297.1.

497   Hennon, C. C., C. N. Helms, K. R. Knapp, and A. R. Bowen (2011), An Objective

498   Algorithm for Detecting and Tracking Tropical Cloud Clusters: Implications for

499   Tropical Cyclogenesis Prediction, *J. Atmos. Ocean. Tech.*, *28*(8), 1007–1018,

500   doi:10.1175/2010JTECHA1522.1.

501   Hoskins, B. J., and K. I. Hodges (2002), New perspectives on the Northern Hemisphere

502   winter storm tracks, *Atmos. Sci*, *59*(6), 1041–1061.

503   Houze, R. A., Jr., K. L. Rasmussen, M. D. Zuluaga, and S. R. Brodzik (2015), The

504   variable nature of convection in the tropics and subtropics: A legacy of 16 years of

505   the Tropical Rainfall Measuring Mission (TRMM) satellite. *Rev. Geophys*., 53,

506   doi:10.1002/2015RG000488.

507   Hou, A. Y., R. K. Kakar, S. Neeck, A. A. Azarbarzin, C. D. Kummerow, M. Kojima, R.

508   Oki, K. Nakamura, and T. Iguchi (2013), The Global Precipitation Measurement

509   Mission, *Bull. Amer. Meteor. Soc.*, *95*(5), 701–722, doi:10.1175/BAMS-D-13-

510   00164.1.

511   Hsu, K., H. V. Gupta, X. Gao, and S. Sorooshian (1999), Estimation of physical variables

512   from multichannel remotely sensed imagery using a neural network: Application to

513   rainfall estimation, *Water Resour. Res.*, *35*(5), 1605–1618,

514   doi:10.1029/1999WR900032.

515   Huffman, G.J., D. Bolvin, D. Braithwaite, K. Hsu, R. Joyce, and P. Xie (2013). NASA

516   Global Precipitation Measurement (GPM) Integrated Multi-satellitE Retrievals for

517   GPM (IMERG). Algorithm Theoretical Basis Doc., version 4.1, NASA, 29 pp.

518   [http://pmm.nasa.gov/sites/default/files/document_files/IMERG_ATBD_V4.1.pdf.]

519   Huffman, G. J., D. T. Bolvin, E. J. Nelkin, D. B. Wolff, R. F. Adler, G. Gu, Y. Hong, K.

520   P. Bowman, and E. F. Stocker (2007), The TRMM Multisatellite Precipitation

521   Analysis (TMPA): Quasi-global, multiyear, combined-sensor precipitation estimates

522   at fine scales, *Journal of Hydrometeorology*, *8*(1), 38–55.

523   Janowiak, J. E., R. J. Joyce, and Y. Yarosh (2001), A Real–Time Global Half–Hourly

524   Pixel–Resolution Infrared Dataset and Its Applications, *Bull. Amer. Meteor. Soc.*,

525   *82*(2), 205–217, doi:10.1175/1520-0477.

526   Joyce, R. J., J. E. Janowiak, P. A. Arkin, and P. Xie (2004), CMORPH: A method that

527   produces global precipitation estimates from passive microwave and infrared data at

528   high spatial and temporal resolution, *Journal of Hydrometeorology*, *5*(3), 487–503.

529   Kikuchi, K., and B. Wang (2008), Diurnal Precipitation Regimes in the Global Tropics*,

530   *Journal of Climate*, *21*(11), 2680–2696, doi:10.1175/2007JCLI2051.1.

531   Kubota, T., and S. Shige (2007), Global Precipitation Map Using Satellite-Borne

532   Microwave Radiometers by the GSMaP Project: Production and Validation, *IEEE*

533   *Trans. Geosci. Remote Sens.*, *45*(7), 2259 – 2275, doi:10.1109/TGRS.2007.895337.

534   Kummerow, C. et al. (2000), The Status of the Tropical Rainfall Measuring Mission

535   (TRMM) after Two Years in Orbit, *J. Appl. Meteor.*, *39*(12), 1965–1982,

536   doi:10.1175/1520-0450(2001)040<1965:TSOTTR>2.0.CO;2.

537   Kunkel, K. E., T. R. Karl, D. R. Easterling, K. Redmond, J. Young, X. Yin, and P.

538   Hennon (2013), Probable maximum precipitation and climate change, *Geophys. Res.*

539   *Lett.*, *40*(7), 1402–1408, doi:10.1002/grl.50334.

540   Laing, A. G., and J. Michael Fritsch (1997), The global population of mesoscale

541   convective complexes, *Q.J.R. Meteorol. Soc.*, *123*(538), 389–405,

542   doi:10.1002/qj.49712353807.

543   Lakshmanan, V., K. Hondl, and R. Rabin (2009), An Efficient, General-Purpose

544   Technique for Identifying Storm Cells in Geospatial Images, *J. Atmos. Ocean.*

545   *Technol.*, *26*(3), 523–537, doi:10.1175/2008JTECHA1153.1.

546   Li, J., K. Hsu, A. AghaKouchak, and S. Sorooshian (2015), An object-based approach for

547   verification of precipitation estimation, *International Journal of Remote Sensing*,

548   *36*(2), 513–529, doi:10.1080/01431161.2014.999170.

549   Liu, C., E. J. Zipser, D. J. Cecil, S. W. Nesbitt, and S. Sherwood (2008), A Cloud and

550   Precipitation Feature Database from Nine Years of TRMM Observations, *J. Appl.*

551   *Meteor. Climatol.*, *47*(10), 2712–2728, doi:10.1175/2008JAMC1890.1.

552   Liu, C., and E. J. Zipser (2009), "Warm Rain" in the Tropics: Seasonal and Regional

553   Distributions Based on 9 yr of TRMM Data, *J. Climate*, *22*(3), 767–779,

554   doi:10.1175/2008JCLI2641.1.

555   Liu, C., and E. J. Zipser (2015), The global distribution of largest, deepest, and most

556   intense precipitation systems: largest, deepest and strongest storms, *Geophys. Res.*

557   *Lett.*, *42*(9), doi:10.1002/2015GL063776.

558   Lovejoy, S., and D. Schertzer (2006), Multifractals, cloud radiances and rain, *J. Hydrol.*,

559   *322*(1-4), 59–88, doi:10.1016/j.jhydro1.2005.02.042.

560   Machado, L. A. T., M. Desbois, and J.-P. Duvel (1992), Structural Characteristics of

561   Deep Convective Systems over Tropical Africa and the Atlantic Ocean, *Monthly*

562   *Weather Review*, *120*(3), 392–406, doi:10.1175/1520-

563   0493(1992)120<0392:SCODCS>2.0.CO;2.

564   Machado, L. A. T., W. B. Rossow, R. L. Guedes, and A. W. Walker (1998), Life cycle

565   variations of mesoscale convective systems over the Americas, *Mon. Weather Rev.*,

566   *126*(6), 1630–1654.

567   Machado, L. A. T., and H. Laurent (2004), The convective system area expansion over

568   Amazonia and its relationships with convective system life duration and high-level

569   wind divergence, *Monthly weather review*, *132*(3), 714–725.

570   Maddox, R. A. (1980), Meoscale Convective Complexes, *Bull. Amer. Meteor. Soc.*,

571   *61*(11), 1374–1387, doi:10.1175/1520-0477.

572   Mapes, B. E., and R. A. Houze (1993), Cloud Clusters and Superclusters over the

573   Oceanic Warm Pool, *Mon. Weather Rev.*, *121*(5), 1398–1416, doi:10.1175/1520-0493.

574   Morel, C., and S. Senesi (2002), A climatology of mesoscale convective systems over

575   Europe using satellite infrared imagery. II: Characteristics of European mesoscale

576   convective systems, *Q.J.R. Meteorol. Soc.*, *128*(584), 1973–1995,

577   doi:10.1256/003590002320603494.

578   Neu, U. et al. (2013), IMILAST: A Community Effort to Intercompare Extratropical

579   Cyclone Detection and Tracking Algorithms, *Bull. Amer. Meteor. Soc.*, *94*(4), 529–

580   547, doi:10.1175/BAMS-D-11-00154.1.

581   Parzen, E. (1962), On Estimation of a Probability Density Function and Mode, *Ann. Math.*

582   *Statist.*, *33*(3), 1065–1076, doi:10.1214/aoms/1177704472.

583   Rosenblatt, M. (1956), Remarks on Some Nonparametric Estimates of a Density Function,

584   *Ann. Math. Statist.*, *27*(3), 832–837, doi:10.1214/aoms/1177728190.

585   Sinclair, M. R. (1994), An Objective Cyclone Climatology for the Southern Hemisphere,

586   *Mon. Wea. Rev.*, *122*(10), 2239–2256, doi:10.1175/1520-0493.

587   Stephens, G. L., T. L'Ecuyer, R. Forbes, A. Gettlemen, J.-C. Golaz, A. Bodas-Salcedo, K.

588   Suzuki, P. Gabriel, and J. Haynes (2010), Dreary state of precipitation in global

589   models, *J. Geophys. Res.*, *115*, D24211, doi:10.1029/2010JD014532.

590   Tadesse, A., and E. N. Anagnostou (2009), The Effect of Storm Life Cycle on Satellite

591   Rainfall Estimation Error, *J. Atmos. Ocean.*, *26*(4), 769–777,

592   doi:10.1175/2008JTECHA1129.1.

593   Teng, H.-F., C.-S. Lee, and H.-H. Hsu (2014), Influence of ENSO on formation of

594   tropical cloud clusters and their development into tropical cyclones in the western

595   North Pacific: Influence of ENSO on TCC Formation, *Geophysical Research Letters*,

596   *41*(24), 9120–9126, doi:10.1002/2014GL061823.

597   Thorncroft, C., and K. Hodges (2001), African Easterly Wave Variability and Its

598   Relationship to Atlantic Tropical Cyclone Activity, *J. Climate*, *14*(6), 1166–1179,

599   doi:10.1175/1520-0442(2001)014<1166:AEWVAI>2.0.CO;2.

600   Velasco, I., and J. Fritsch (1987), Mesoscale Convective Complexes in the America, *J.*

601   *Geophys. Res.-Atmos.*, *92*(D8), 9591–9613, doi:10.1029/JD092iD08p09591.

602   Vila, D. A., L. A. T. Machado, H. Laurent, and I. Velasco (2008), Forecast and Tracking

603   the Evolution of Cloud Clusters (ForTraCC) using satellite infrared imagery:

604   Methodology and validation, *Wea. Forecasting*, *23*(2), 233–245.

605   Westra, S., H. J. Fowler, J. P. Evans, L. V. Alexander, P. Berg, F. Johnson, E. J. Kendon,

606   G. Lenderink, and N. M. Roberts (2014), Future changes to the intensity and

607   frequency of short-duration extreme rainfall, *Rev. Geophys.*, *52*(3), 2014RG000464,

608   doi:10.1002/2014RG000464.

609   Wilks, D. S. (2011), *Statistical methods in the atmospheric sciences*, International

610   geophysics series v. 100, 3rd ed., Elsevier/Academic Press, Amsterdam ; Boston.

611   Williams, M., and R. A. Houze (1987), Satellite-Observed Characteristics of Winter

612   Monsoon Cloud Clusters, *Mon. Weather Rev.*, *115*(2), 505–519, doi:10.1175/1520-

613   0493.

614   Xie, P., and A.-Y. Xiong (2011), A conceptual model for constructing high-resolution

615   gauge-satellite merged precipitation analyses, *J. Geophys. Res.*, *116*(D21), D21106,

616   doi:10.1029/2011JD016118.

617   Zahraei, A., K. Hsu, S. Sorooshian, J. J. Gourley, Y. Hong, and A. Behrangi (2013),

618   Short-term quantitative precipitation forecasting using an object-based approach, *J.*

619   *Hydrol.*, *483*, 1–15, doi:10.1016/j.jhydrol.2012.09.052.

620   Zipser, E. J., D. J. Cecil, C. Liu, S. W. Nesbitt, and D. P. Yorty (2006), Where are the

621   most intense thunderstorms on earth?, *Bull. Amer. Meteorol. Soc.*, *87*(8), 1057,

622   doi:10.1175/BAMS-87-8-1057.

623   Zolina, O., and S. K. Gulev (2002), Improving the Accuracy of Mapping Cyclone

624   Numbers and Frequencies, *Mon. Wea. Rev.*, *130*(3), 748–759, doi:10.1175/1520-0493.

625

a)
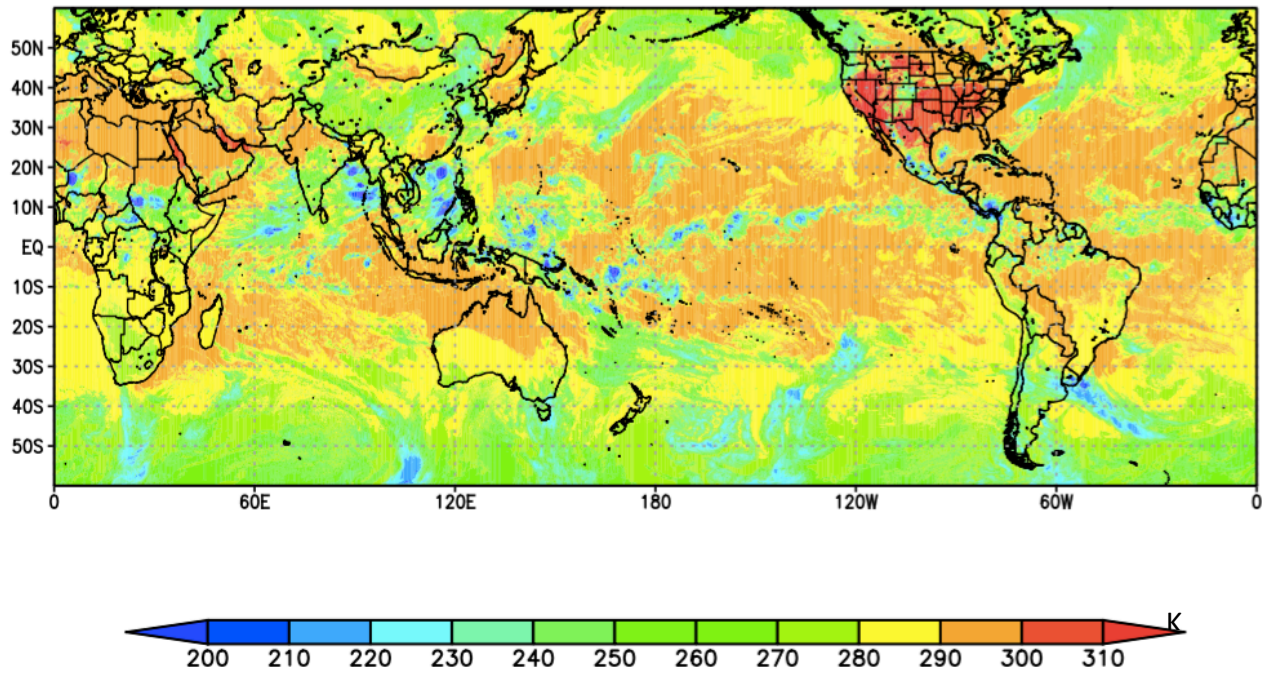
b)
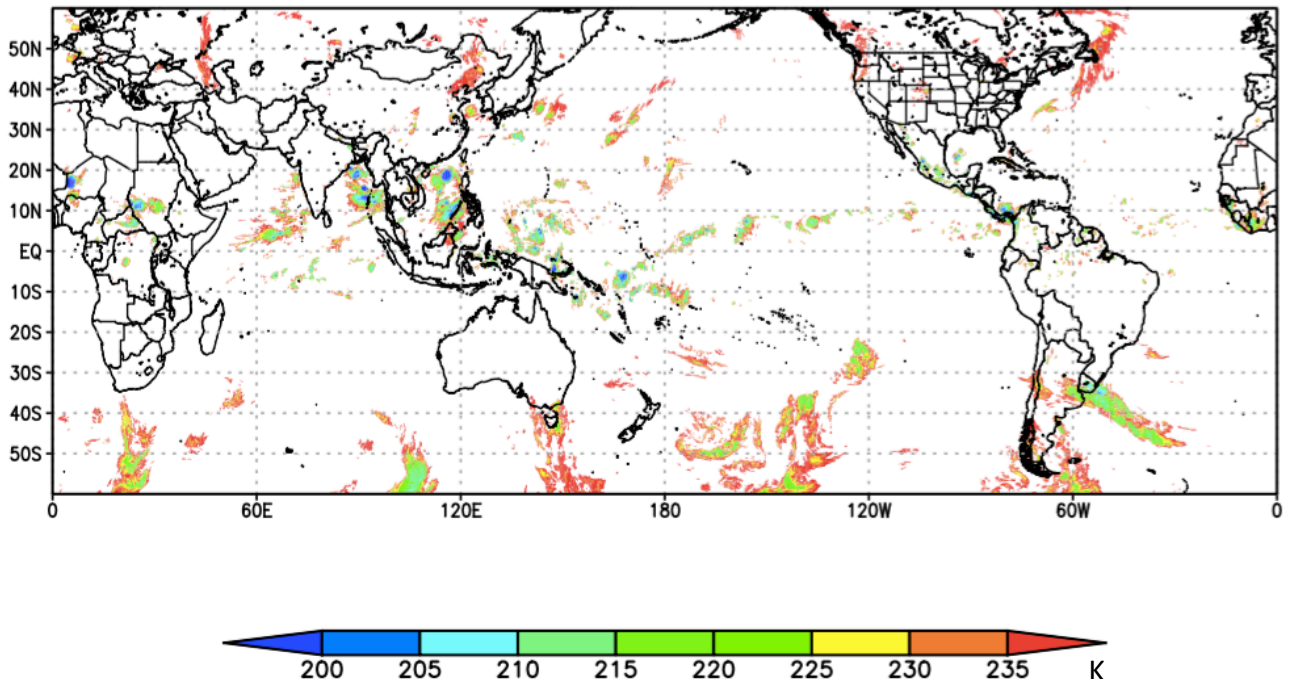
Figure 1. (a) Globally merged map of IR brightness temperature from NCEP/CPC Cloud brightness temperature dataset for 23:00 GMT June 28, 2012. (b) Cloud clusters captured by ForTraCC after applying temperature and size thresholds. Shading represents cloud brightness temperature.
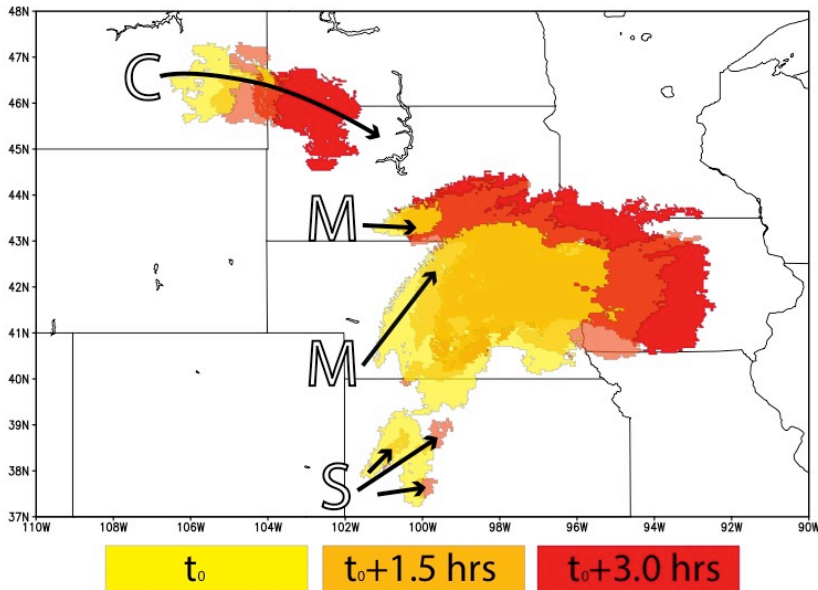
Figure 2. Schematic of area-overlap handling of continuous systems (c), merging systems (m), and splitting systems (s). The image was taken of thunderstorms developing over the American Midwest beginning at 3:00pm EST on June 30, 2012. Yellow represents the initial time, orange 1.5 hours later, and red 3.0 hours after initial detection.
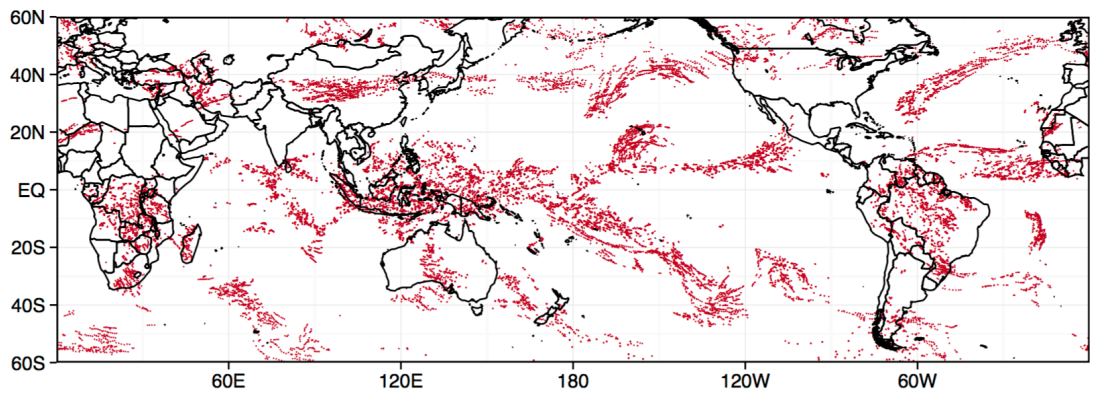
Figure 3. Cloud cluster tracks from Dec 1-4, 2001 produced from using the ForTrACC algorithm. A few days of tracking yield a large number of clusters and their movement begins to trace out large-scale atmospheric patterns.
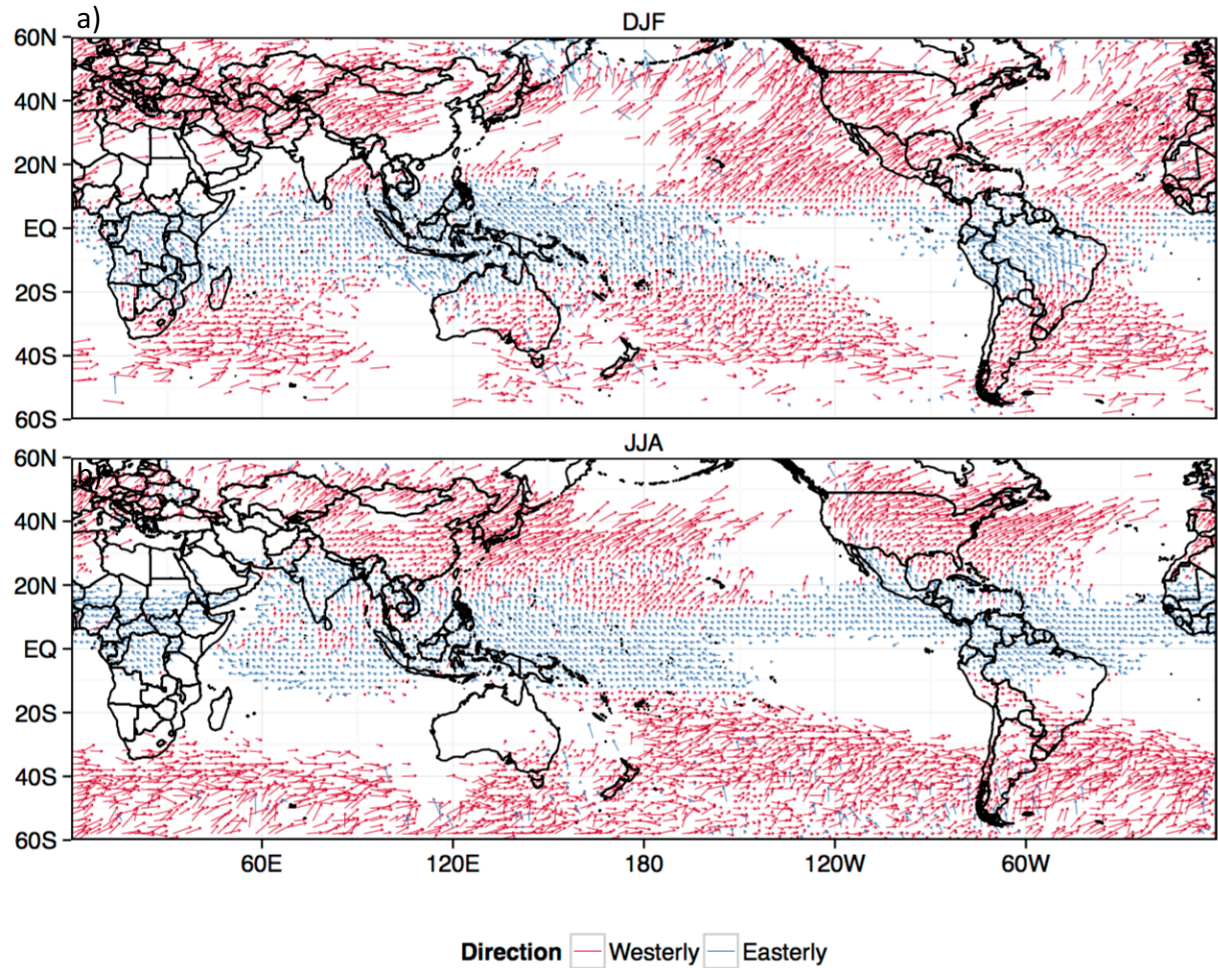
Figure 4. Climatology of cloud cluster trajectories in (a) DJF and (b) JJA, 2002-2012 with 6-9 hour lifetimes binned by 2° x 2°. Lines show average displacement of all cloud clusters that initiated at the same point over the 11-year period studied. Coloring indicates net zonal movement of clusters. Grid boxes with fewer than five initiations were not displayed.
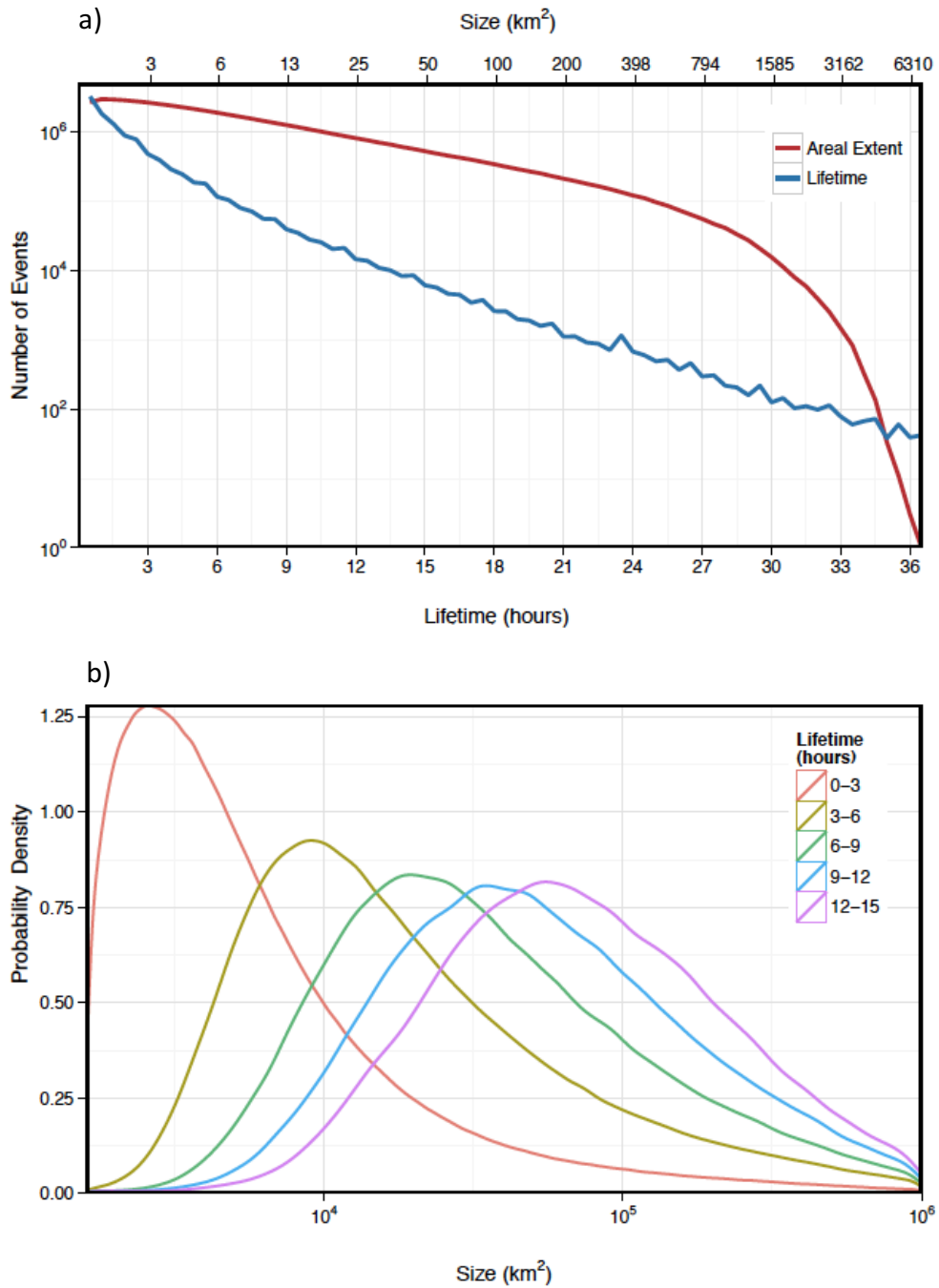
Figure 5. (a) Number of detected events globally by lifetime and size for the entire record. (b) The kernel density estimate of cloud clusters at their maximum areal extent for each lifetime group over the entire study period (DJF and JJA, 2002-2012).
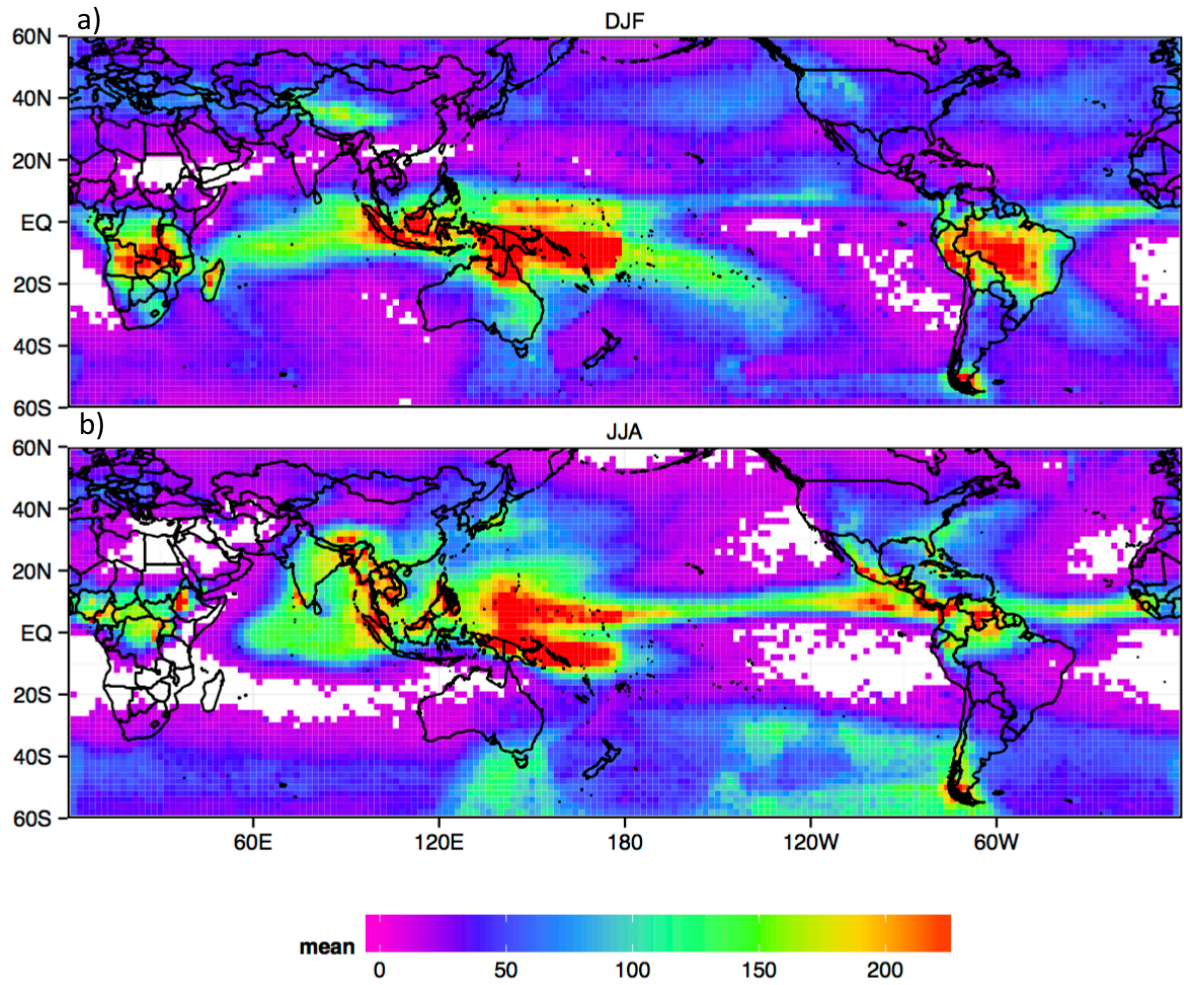
Figure 6. Mean seasonal frequency of clusters for (a) DJF and (b) JJA at their maximum areal extent. The figure shows the average seasonal count of events over the study period, binned by 2° x 2° latitude-longitude. Warmer colors represent higher counts while cooler colors represent fewer observations. White grid boxes have ten or fewer cloud clusters across the 11 year period.
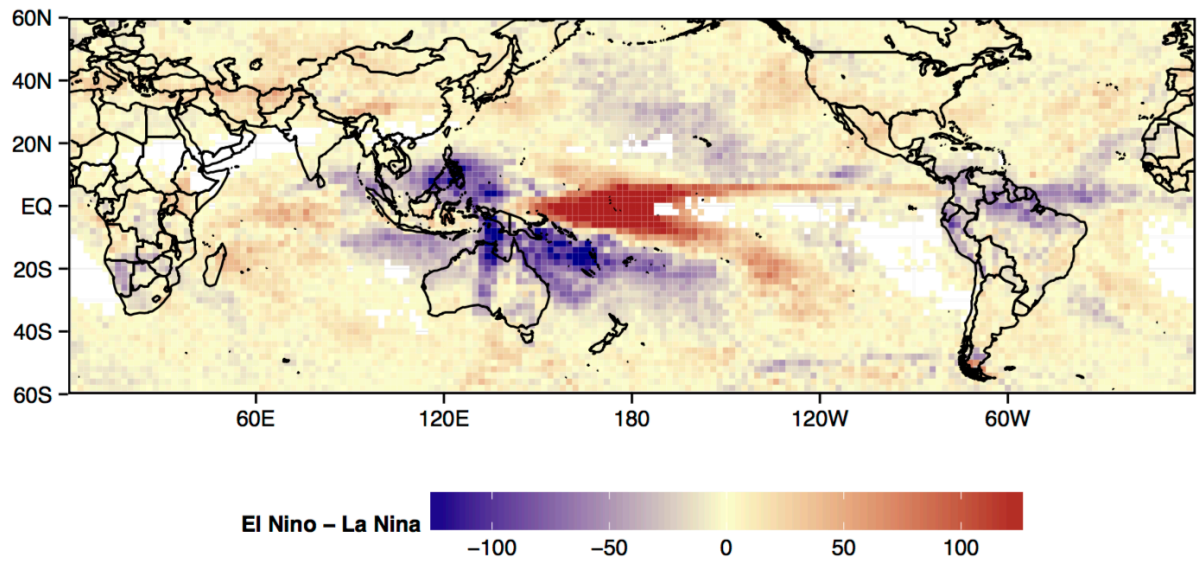
Figure 7. The composite of the 11-year DJF mean annual frequency of cloud cluster overpasses for El Niño and La Niña, binned by 2° x 2° latitude-longitude, at their maximum areal extent. Warm or cool event years were selected based on the NINO3.4 sea surface temperature anomaly index. White grid boxes have three or fewer cloud clusters.
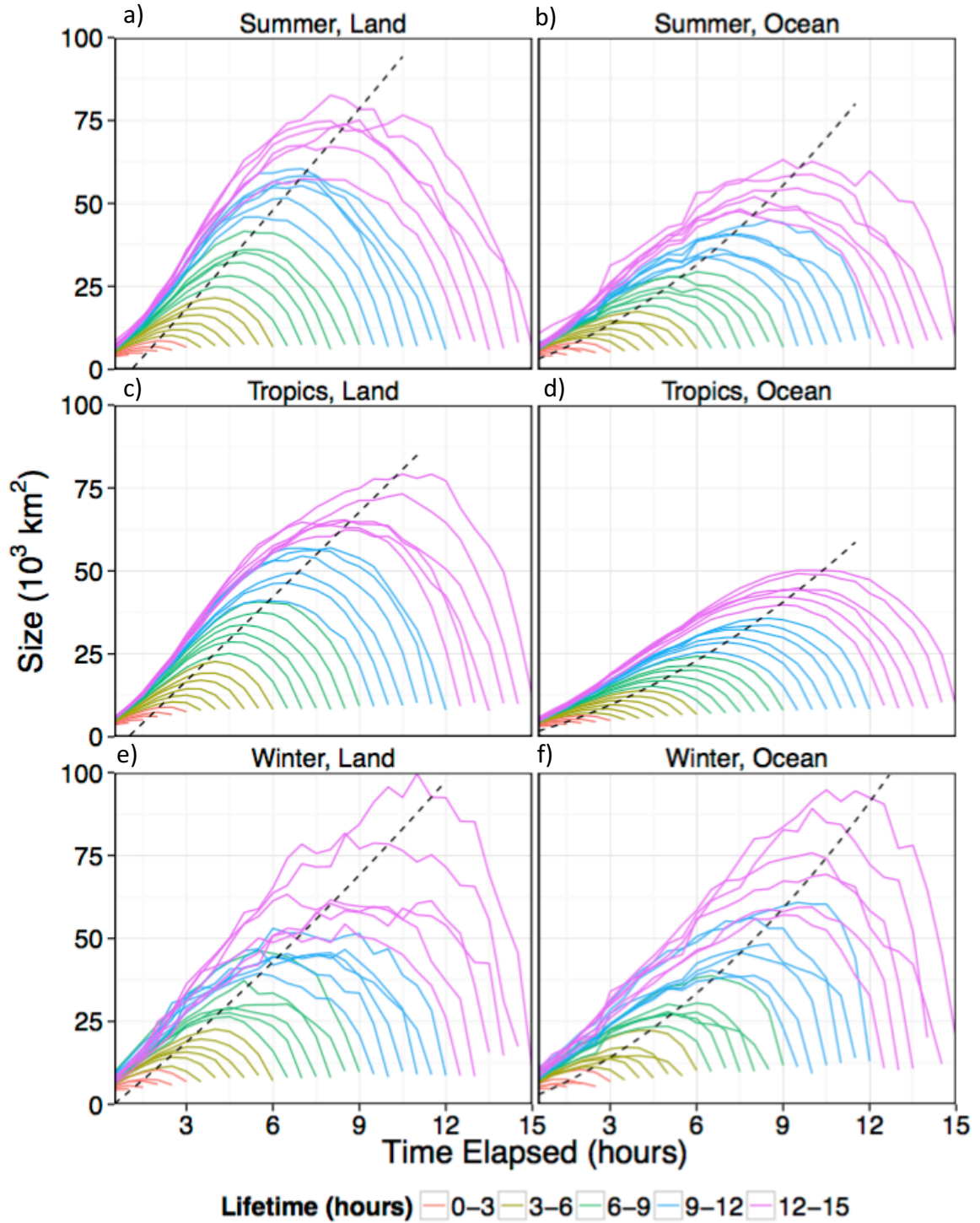
Figure 8. The global average life cycle evolution for new cloud clusters with varying life times. Each curve represents the average properties of millions of clusters grouped by life span. The shortest lines are short-lived events longer lines are long-lived. Curves show how the size changes as a function of the clusters' lifetime. Dashed curve is a regression fitted to the maximum of each curve. Seasons are defined by the ±25° latitude line.
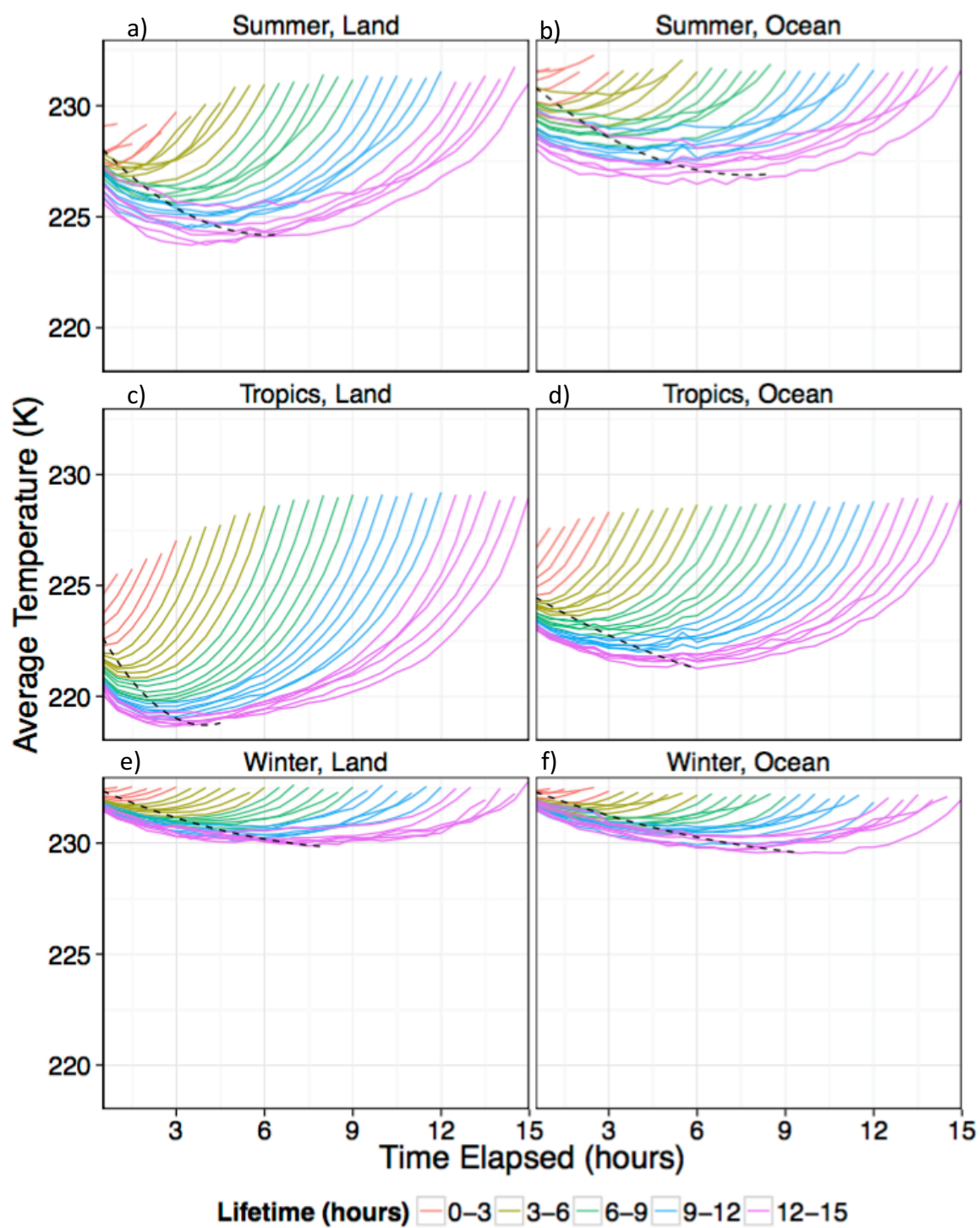
Figure 9. Same as Figure 8, but showing how the average brightness temperature changes as a function of time and lifetime.
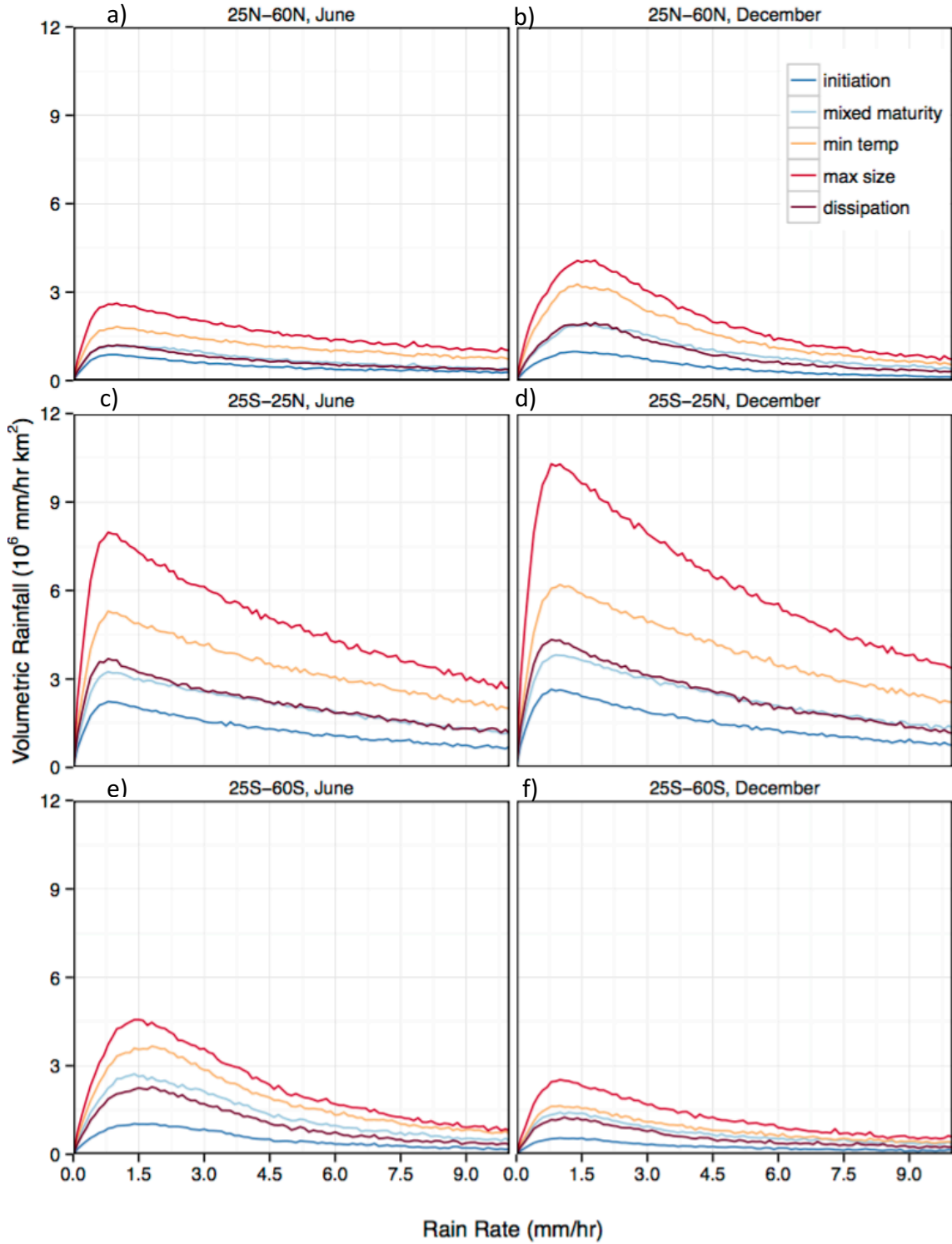
Figure 10. Total instantaneous rainfall contribution as a function of rain rate captured by clusters in the (a, b) Northern Hemisphere, (c, d) tropics, and (e, f) Southern Hemisphere in June and December 2014. The distribution is based on coincident cloud clusters and passive microwave-based rainfall estimates from the IMERG dataset.
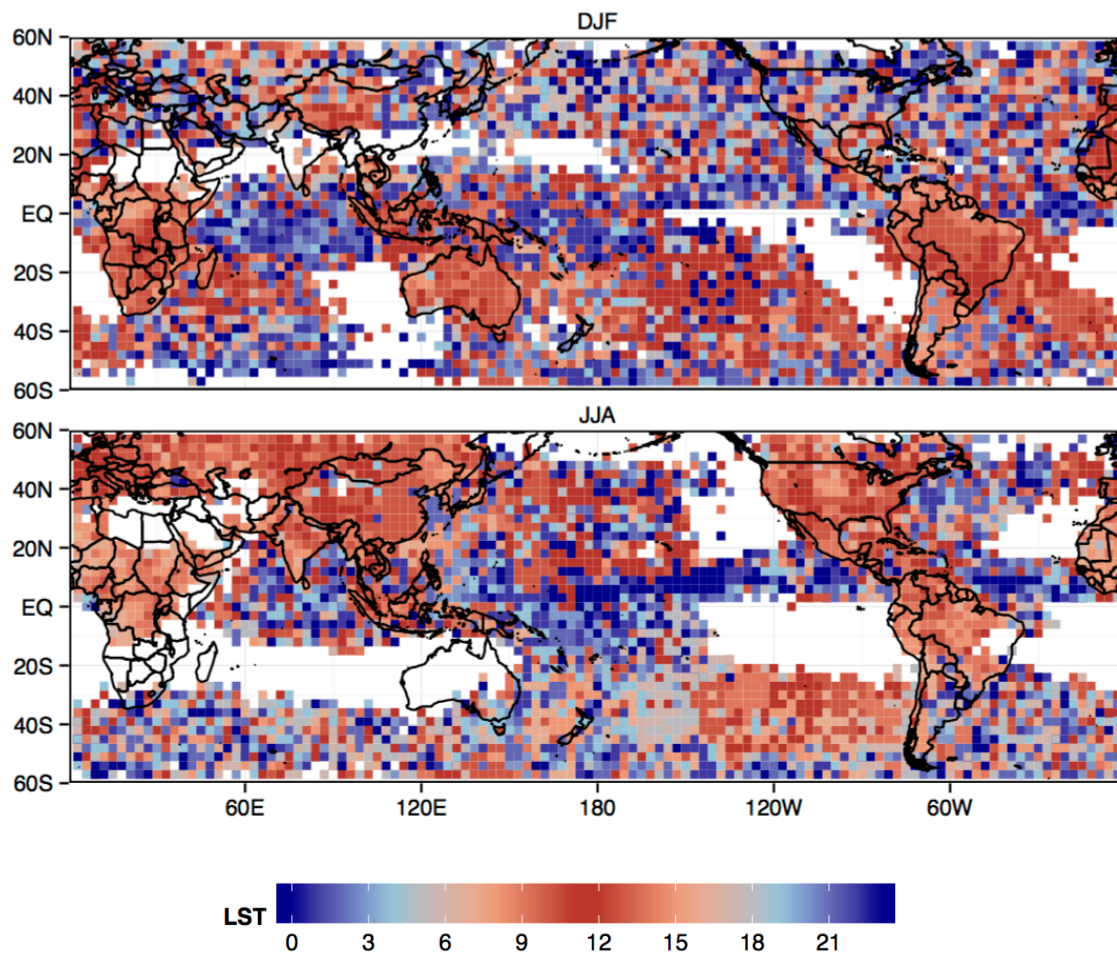
Figure 11. Diurnal variation in local solar time (LST) cloud cluster initiation for (a) DJF and (b) JJA, binned by 2° x 2° latitude-longitude. Each box shows the timing of maximum occurrence of cluster formation for the 11-year record. Only clusters with a lifetime greater than two hours are included.
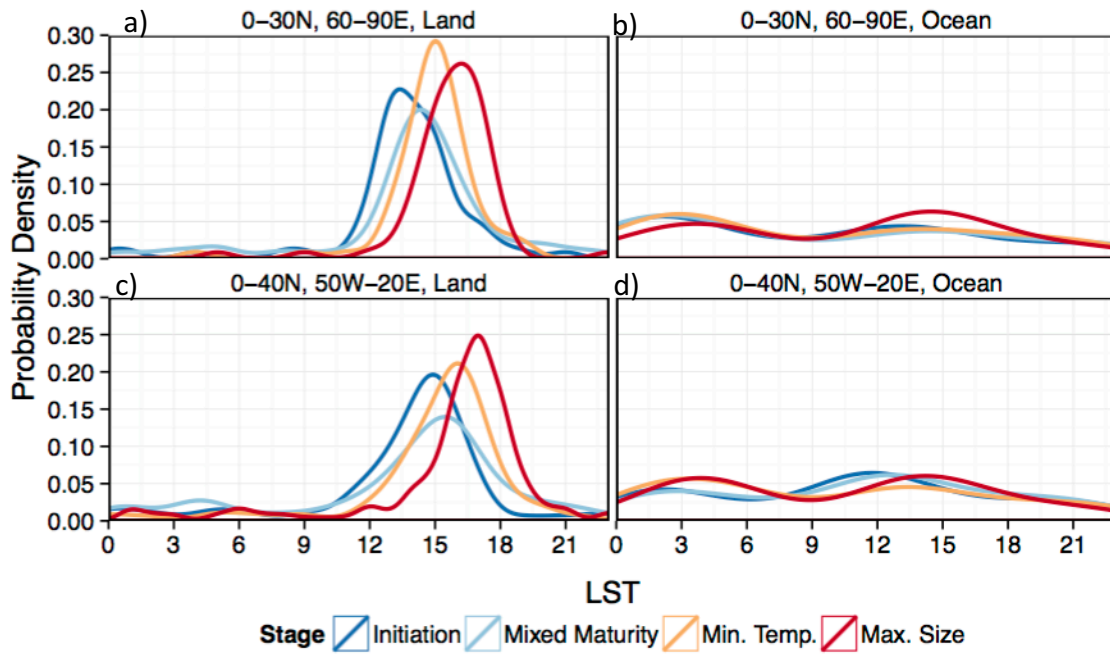
Figure 12. The kernel density of local solar time of the life cycle stage in two regions, 0°-30°N and 60°-90°E (South Asia) and 0-40°N, 50°W-20°E (West Africa).
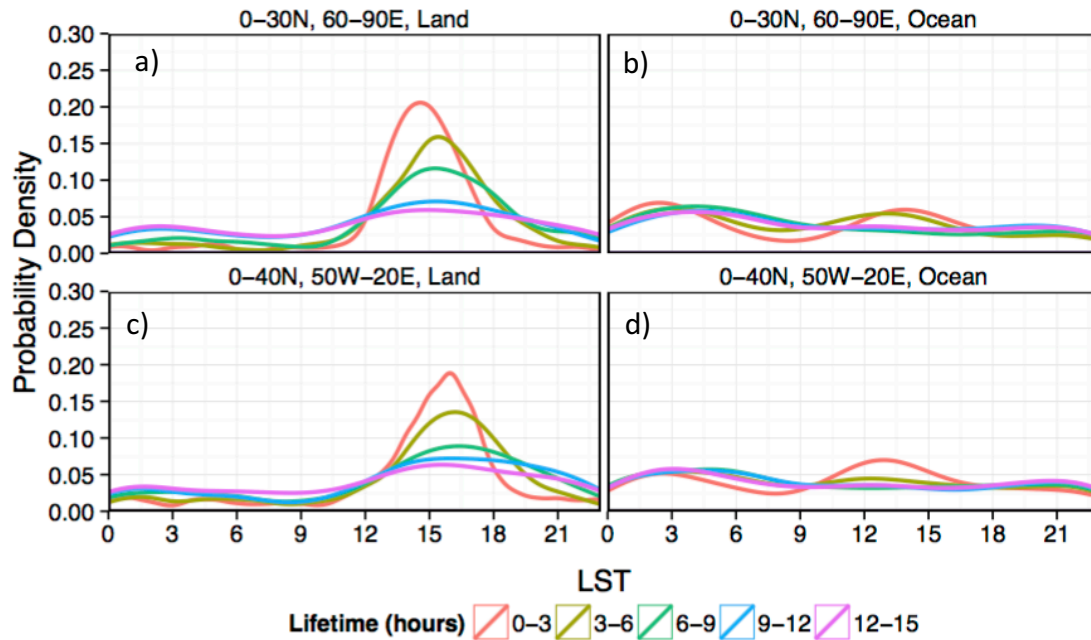

Figure 13. The kernel density of local solar time of initiation in three-hourly lifetime bins for two regions, 0°-30°N and 60°-90°E (South Asia) and 0-40°N, 50°W-20°E (West Africa).